

BASIC STUDY ON THE DYNAMIC SOIL-STRUCTURE INTERACTION*

*Koichi Akai***

*Masayuki Hori****

1. INTRODUCTION

It was reported that, in the Niigata Earthquake 1964, serious damages took place in the ground at the neighbourhood of the base of structures, compared with those of structures on the ground surface¹⁾. Though these phenomena are based on the special geological condition in Niigata, of cause, it may be also due to the existence of structures on or in the ground itself, a large impact applying to the base of structures. A seismic wave propagating through the ground to the base of structures causes reflection and divergence at the boundary, and the incident and reflected stresses are superposed with each other, thus causing a large stresses in the ground supporting structures.

When dealing with aseismicity of structures, therefore, it becomes necessary to analyze the problem in view of wave propagation to the soil-structure system. This treatment is not limited only to the structure on the ground surface, but also to the underground structure such as culverts, footings or pile foundations and their surrounding ground, in order to investigate their dynamic behavior or failure mechanism under seismic condition.

The dynamic interaction between structure and soil ground under seismic condition complicates the solution of problem so much, because the dynamic response of both structure and ground has not been solved comprehensively. For this reason the interaction problem will be treated as the simplest form in the present paper. A model cylinder buried in the cohesive soil subjected by the dilatational stress wave is simulated as a structure under seismic condition, and reflection and divergence at the cylindrical surface are investigated both theoretically and experimentally.

Comprehensive research on the dynamic soil-structure interaction should be orientated to the problem under the distortional stress wave from which the main part of actual earthquake motion is constituted. This remains still for us as the further study.

2. THEORETICAL BACKGROUND

First consider a plane step compressional stress wave as Fig. 1 propagating in a semi-infinite medium of which constitutive curve is expressed by a bi-linear model in Fig. 2 and reflected by its rigid dense boundary as shown in Fig. 3²⁾. In this figure an elastic dilatational wave (P-wave) penetrates into the medium with a celerity c_{11} and an incidental angle θ_1 . By reflecting at the boundary

* Presented at the 24th Annual Meeting of J.S.C.E., Sept., 1969

** Dr. Eng., Professor of Civil Engineering, Kyoto University

*** Graduate course student, Kyoto University

surface, there occurs an additional loading at the neighbourhood of the boundary and, therefore, there propagate a plastic dilatational wave and a plastic distortional

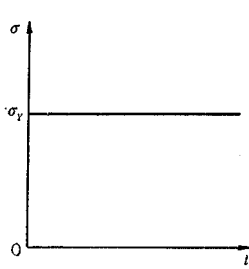


Fig. 1 Step compressional stress wave.

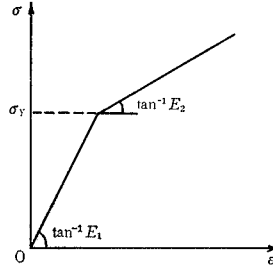


Fig. 2 Stress-strain curve for bi-linear model.

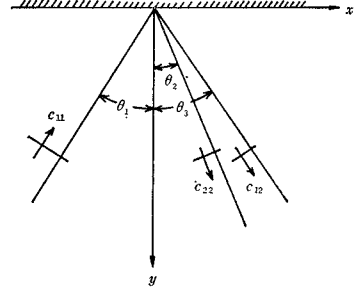


Fig. 3 Reflection of incident P-wave at a rigid boundary.

wave (S-wave) with celerities c_{12} and c_{22} , respectively. Celerities thus defined are represented as follows:

$$\left. \begin{aligned} c_{11}^2 &= \frac{\lambda_1 + 2\mu_1}{\rho} = \frac{E_1(1-\nu_1)}{\rho(1+\nu_1)(1-2\nu_1)} \\ c_{12}^2 &= \frac{\lambda_2 + 2\mu_2}{\rho} = \frac{E_2(1-\nu_2)}{\rho(1+\nu_2)(1-2\nu_2)} \\ c_{22}^2 &= \frac{\mu_2}{\rho} = \frac{E_2}{2\rho(1+\nu_2)} \end{aligned} \right\} \quad (1)$$

where ρ denotes the density of medium, λ and μ Lamé's constants and ν Poisson's ratio. Then, the incident motion is given as:

$$\nabla^2 \phi = \frac{1}{c_{11}^2} \frac{\partial^2 \phi}{\partial t^2} \quad (2)$$

where ϕ denotes the deformation potential defined as

$$u_x = \frac{\partial \phi}{\partial x}, \quad u_y = \frac{\partial \phi}{\partial y} \quad (3)$$

According to the theory of elasticity, stress components are expressed as³⁾:

$$\left. \begin{aligned} \sigma_x &= \lambda_1 \nabla^2 \phi + 2\mu_1 \frac{\partial^2 \phi}{\partial x^2} \\ \sigma_y &= \lambda_1 \nabla^2 \phi + 2\mu_1 \frac{\partial^2 \phi}{\partial y^2} \\ \tau_{xy} &= 2\mu_1 \frac{\partial^2 \phi}{\partial x \partial y} \end{aligned} \right\} \quad (4)$$

Solving the fundamental equation (2) with the boundary condition and the initial condition, the incident potential may be taken as:

$$\phi^{(i)} = \frac{p}{2\rho} \left(t - \frac{x \sin \theta_1 - y \cos \theta_1}{c_{11}} \right)^2 H \left(t - \frac{x \sin \theta_1 - y \cos \theta_1}{c_{11}} \right) \quad (5)$$

where p is the intensity of the input wave and H the Heaviside's step function.

The origin of time is taken as the instance when the wave front has reached the rigid boundary surface⁴⁾.

From Eqs. (4) and (5) the incident stresses are given as:

$$\left. \begin{aligned} \sigma_x &= \frac{\lambda_1 + 2\mu_1 \sin^2 \theta_1}{\lambda_1 + 2\mu_1} p \cdot H \left(t - \frac{x \sin \theta_1 - y \cos \theta_1}{c_{11}} \right) \\ \sigma_y &= \frac{\lambda_1 + 2\mu_1 \cos^2 \theta_1}{\lambda_1 + 2\mu_1} p \cdot H \left(t - \frac{x \sin \theta_1 - y \cos \theta_1}{c_{11}} \right) \\ \tau_{xy} &= -\frac{2\mu_1 \sin \theta_1 \cos \theta_1}{\lambda_1 + 2\mu_1} p \cdot H \left(t - \frac{x \sin \theta_1 - y \cos \theta_1}{c_{11}} \right) \end{aligned} \right\} \quad (6)$$

Giving p as the yielding stress of the medium as shown in Fig. 2, it may be verified that the incident stresses, Eq. (6), just plasticize the medium before the reflection takes place. Accordingly the reflected motion is given by:

$$\mu_2 u_{i,jj}^{(2)} + (\lambda_2 + \mu_2) u_{j,ji}^{(2)} + \sigma_{ij,j}^{(01)} = \rho \frac{\partial^2 u_i^{(2)}}{\partial t^2} \quad (7)$$

where the suffix i denotes the active index, j the dummy index, and symbols (01), (2) indicate the elastic region and the plastic region, respectively.

Substituting Eq. (6) into Eq. (7), one obtains

$$\mu_2 u_{i,jj}^{(2)} + (\lambda_2 + \mu_2) u_{j,ji}^{(2)} = \rho \frac{\partial^2 u_i^{(2)}}{\partial t^2} \quad (8)$$

Then, let us define the reflected deformation potential $\phi^{(r)}$, $\psi^{(r)}$ as follows:

$$u_x = \frac{\partial \phi^{(r)}}{\partial x} + \frac{\partial \psi^{(r)}}{\partial y}, \quad u_y = \frac{\partial \phi^{(r)}}{\partial y} - \frac{\partial \psi^{(r)}}{\partial x} \quad (9)$$

As similar as in the elastic case, Eq. (8) reduces to

$$\nabla^2 \phi^{(r)} = \frac{1}{c_{12}^2} \frac{\partial^2 \phi^{(r)}}{\partial t^2}, \quad \nabla^2 \psi^{(r)} = \frac{1}{c_{22}^2} \frac{\partial^2 \psi^{(r)}}{\partial t^2} \quad (10)$$

A solution of these equations may be taken as:

$$\left. \begin{aligned} \phi^{(r)} &= \frac{A}{2\rho} \left(t - \frac{x \sin \theta_3 + y \cos \theta_3}{c_{12}} \right)^2 H \left(t - \frac{x \sin \theta_3 + y \cos \theta_3}{c_{12}} \right) \\ \psi^{(r)} &= \frac{B}{2\rho} \left(t - \frac{x \sin \theta_2 + y \cos \theta_2}{c_{22}} \right)^2 H \left(t - \frac{x \sin \theta_2 + y \cos \theta_2}{c_{22}} \right) \end{aligned} \right\} \quad (11)$$

where A and B are reflection coefficients to be determined from boundary conditions:

$$u_x^{(i)} + u_x^{(r)} \Big|_{y=0} = u_y^{(i)} + u_y^{(r)} \Big|_{x=0} = 0 \quad (12)$$

From Eqs. (3), (4), (9), (11) and the boundary conditions (12), we obtain Snell's law and the reflection coefficients as:

$$\frac{\sin \theta_1}{c_{11}} = \frac{\sin \theta_2}{c_{22}} = \frac{\sin \theta_3}{c_{12}} \quad (13)$$

$$\left. \begin{aligned} R_{pp} &= \frac{A}{\dot{p}} = \frac{\cos(\theta_1 + \theta_2)}{\sin \theta_1 \sin \theta_2 + \frac{c_{11}}{c_{12}} \cos \theta_2 \cos \theta_3} \\ R_{ps} &= \frac{B}{\dot{p}} = -\frac{c_{22}}{c_{11}} \frac{\sin \theta_1 \left(\frac{c_{11}}{c_{12}} \cos \theta_3 + \cos \theta_1 \right)}{\sin \theta_1 \sin \theta_2 + \frac{c_{11}}{c_{12}} \cos \theta_2 \cos \theta_3} \end{aligned} \right\} \quad (14)$$

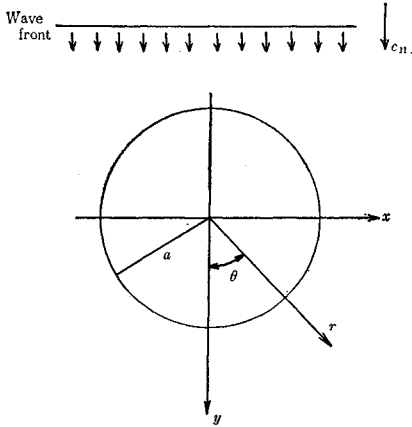


Fig. 4 Rigid perfectly dense cylinder subjected to stress wave.

Fitting to the experimental condition described later, consider a plane compressional step wave propagating at the yield stress of the medium reflected by a rigid perfectly dense cylinder as shown in Fig. 4. Still taking the origin of time as the instance when the wave front has just reached the crown of cylindrical structure, the incident potential is given in the following equation:

$$\begin{aligned} \phi^{(i)} &= \frac{\dot{p}}{2\rho} \left(t - \frac{x+a}{c_{11}} \right)^2 H \left(t - \frac{x+a}{c_{11}} \right) \\ &= \frac{\dot{p}}{2\rho} \left(t - \frac{a+r \cos \theta}{c_{11}} \right)^2 H \left(t - \frac{a+r \cos \theta}{c_{11}} \right) \end{aligned} \quad (15)$$

As has mentioned before the incident wave is reflected as a compressional and a shear wave. The reflected deformation potential may be taken as:

$$\left. \begin{aligned} \phi^{(r)} &= \frac{\dot{p}}{2\rho} D_{pp} R_{pp} \left\{ t - \frac{R_p}{c_{12}} - \frac{a(1-\cos \eta_p)}{c_{11}} \right\}^2 H \left\{ t - \frac{R_p}{c_{12}} - \frac{a(1-\cos \eta_p)}{c_{11}} \right\} \\ \phi^{(s)} &= \frac{\dot{p}}{2\rho} D_{ps} R_{ps} \left\{ t - \frac{R_s}{c_{22}} - \frac{a(1-\cos \eta_s)}{c_{11}} \right\}^2 H \left\{ t - \frac{R_s}{c_{22}} - \frac{a(1-\cos \eta_s)}{c_{11}} \right\} \end{aligned} \right\} \quad (16)$$

where the cylindrical divergence coefficients are*

$$D_{pp} = \sqrt{\frac{f}{f+R_p}}, \quad D_{ps} = \sqrt{\frac{g}{g+R_s}} \quad (17)$$

f, g : radii of curvature of the reflected P- and S-wave fronts on the cylinder,

R_p, R_s : distances along the reflected P- and S-rays to the point of observation,

η_p, η_s : corresponding angles of incidence.

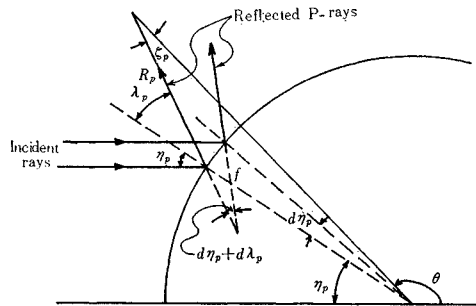


Fig. 5 Interaction geometry for reflected P-wave.

Letting $c_{12}=c_{11}$ and $c_{22}=c_{21}$ the stresses on the boundary are given for the elastic problem, where $c_{21}=\sqrt{\mu_1/\rho}$ denotes the celerity of elastic distortional wave.

* See Appendix

Fig. 5 shows the interaction geometry for the reflected P-wave front. From this figure and Snell's law (13) it follows:

$$\left. \begin{aligned} f &= \frac{a \cos^2 \lambda_p}{\cos \lambda_p + \frac{c_{12}}{c_{11}} \cos \eta_p} \\ \text{Similarly for the reflected S-wave,} \\ g &= \frac{a \cos^2 \lambda_s}{\cos \lambda_s + \frac{c_{22}}{c_{11}} \cos \eta_s} \end{aligned} \right\} \quad (18)$$

where λ_p and λ_s are the angles of reflection of the P- and S-rays for the incident angles η_p and η_s , respectively.

From Eqs. (17) and (18) the divergence coefficients are given as:

$$\left. \begin{aligned} D_{pp} &= \left\{ \frac{a \cos^2 \lambda_p}{R_p \left(\cos \lambda_p + \frac{c_{12}}{c_{11}} \cos \eta_p \right) + a \cos^2 \lambda_p} \right\}^{1/2} \\ D_{ps} &= \left\{ \frac{a \cos^2 \lambda_s}{R_s \left(\cos \lambda_s + \frac{c_{22}}{c_{11}} \cos \eta_s \right) + a \cos^2 \lambda_s} \right\}^{1/2} \end{aligned} \right\} \quad (19)$$

From Eqs. (13) and (14), on the other hand, the reflection coefficients are given as:*

$$\left. \begin{aligned} R_{pp} &= \frac{\cos \eta_p \left\{ 1 - \left(\frac{c_{22}}{c_{11}} \right)^2 \sin^2 \eta_p \right\}^{1/2} - \frac{c_{22}}{c_{11}} \sin^2 \eta_p}{\frac{c_{11}}{c_{12}} \left\{ 1 - \left(\frac{c_{12}}{c_{11}} \right)^2 \sin^2 \eta_p \right\}^{1/2} \left\{ 1 - \left(\frac{c_{22}}{c_{11}} \right)^2 \sin^2 \eta_p \right\}^{1/2} + \frac{c_{22}}{c_{11}} \sin^2 \eta_p} \\ R_{ps} &= -\frac{c_{22}}{c_{11}} \frac{\sin \eta_s \left[\frac{c_{11}}{c_{12}} \left\{ 1 - \left(\frac{c_{12}}{c_{11}} \right)^2 \sin^2 \eta_s \right\}^{1/2} + \cos \eta_s \right]}{\frac{c_{11}}{c_{12}} \left\{ 1 - \left(\frac{c_{12}}{c_{11}} \right)^2 \sin^2 \eta_s \right\}^{1/2} \left\{ 1 - \left(\frac{c_{22}}{c_{11}} \right)^2 \sin^2 \eta_s \right\}^{1/2} + \frac{c_{22}}{c_{11}} \sin^2 \eta_s} \end{aligned} \right\} \quad (20)$$

Transforming Eqs. (8) and (9) into the polar coordinate system and using Eq. (16) for calculating the problem, the reflected stresses are finally given by the following equations to the first order of approximation:

$$\left. \begin{aligned} \sigma_r^{(r)} &= \frac{\lambda_2 + 2\mu_2 \cos^2 \zeta_p}{c_{12}^2} \frac{\rho}{\rho} D_{pp} R_{pp} H \left\{ t - \frac{R_p}{c_{12}} - \frac{a(1 - \cos \eta_p)}{c_{11}} \right\} \\ &\quad - 2\mu_2 \frac{\sin \zeta_s \cos \zeta_s}{c_{22}^2} \frac{\rho}{\rho} D_{ps} R_{ps} H \left\{ t - \frac{R_s}{c_{22}} - \frac{a(1 - \cos \eta_s)}{c_{11}} \right\} \\ \sigma_\theta^{(r)} &= \frac{\lambda_2 + 2\mu_2 \sin^2 \zeta_p}{c_{12}^2} \frac{\rho}{\rho} D_{pp} R_{pp} H \left\{ t - \frac{R_p}{c_{12}} - \frac{a(1 - \cos \eta_p)}{c_{11}} \right\} \\ &\quad + 2\mu_2 \frac{\sin \zeta_s \cos \zeta_s}{c_{22}^2} \frac{\rho}{\rho} D_{ps} R_{ps} H \left\{ t - \frac{R_s}{c_{22}} - \frac{a(1 - \cos \eta_s)}{c_{11}} \right\} \\ \tau_{r\theta}^{(r)} &= \mu_2 \left[\frac{\sin^2 \zeta_s - \cos^2 \zeta_s}{c_{22}^2} \frac{\rho}{\rho} D_{ps} R_{ps} H \left\{ t - \frac{R_s}{c_{22}} - \frac{a(1 - \cos \eta_s)}{c_{11}} \right\} \right. \\ &\quad \left. - \frac{2 \sin \zeta_p \cos \zeta_p}{c_{12}^2} \frac{\rho}{\rho} D_{pp} R_{pp} H \left\{ t - \frac{R_p}{c_{12}} - \frac{a(1 - \cos \eta_p)}{c_{11}} \right\} \right] \end{aligned} \right\} \quad (21)$$

* See Appendix

3. EXPERIMENTAL APPARATUS AND TEST PROCEDURE

3.1 Impact Test

Two kinds of impact test are necessary to investigate the propagation of stress wave through soil and also the diffusion of stress wave at the surface of a cylinder buried in soil sample; those are the tests for soil specimen which contains model cylinder and without cylinder.

(1) Test for clay specimen which does not contain model cylinder

Fig. 6 shows the schematic diagram of the experimental apparatus. Explanation of symbols in this figure is as follows:

S: Clay specimen.

Test specimens were taken out from a clay layer artificially sedimentated and consolidated under the pressure of about 1 kg/cm^2 in a very large vessel (diameter 2.0 m, height 1.5 m). Physical properties of clay are summarized in Table 1. For sampling a sampler made of vinyl-chloride which diameter is 15 cm and length is 90 cm was used. The length of clay specimens was about 45 cm-55 cm. These specimens self-stood vertically as shown in Fig. 6.

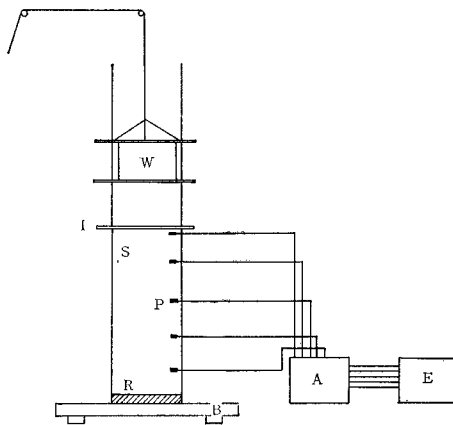


Fig. 6 Impact test apparatus.

R: Reaction end.

When dealing with short specimens encountered in this experiment, one cannot avoid the influence of the reflected wave coming from the reaction end. To minimize this influence a bubbled styrol was used in a series of this test.

B: Supporting frame.

At the centre of the bottom of wooden supporting frame there is a steel plate. Four steel poles of 5 mm diameter stand up from the plate to prevent overturning the clay specimen as well as to guide a drop hammer. These poles fit the clay specimen, nevertheless they do not confine for the specimen to move horizontally. Thus we can treat the analysis under the condition of no lateral confinement.

P: Small pressure gauge.⁵⁾

The gauge was 6 mm in diameter and 0.5 mm in thickness and was stuck on

Table 1 Physical properties of clay specimen.

Specific gravity	2.61
Bulk density	1.96 g/cm^3
Particle composition	
Clay fraction ($<5\mu$)	5%
Silt fraction	72%
Sand fraction	23%
Liquid limit	72.6%
Plasticity index	43.5%
Water content	55-65%

a small brass plate. It had the maximum measuring capacity of 2 kg/cm^2 .

I: Impact end.

In order to obtain a plane compressive stress wave as the input, a wooden plate was fitted directly on the upper end of clay specimen.

W: Falling weight (Photo. 1).

Shot leads were packed in a can vessel. Total weight amounted to 1 750 g and the falling height to 70 cm. The amount of input thus obtained was about 0.3 kg/cm^2 .

A: Amplifier.

E: Electro-magnetic oscilloscope.

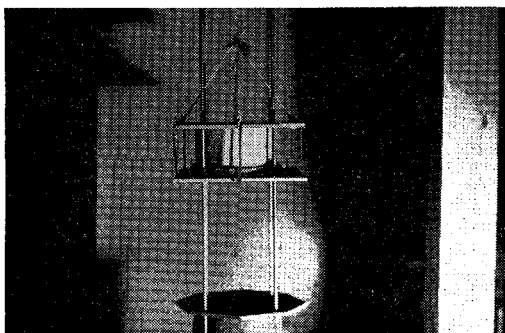


Photo. 1 Falling weight.

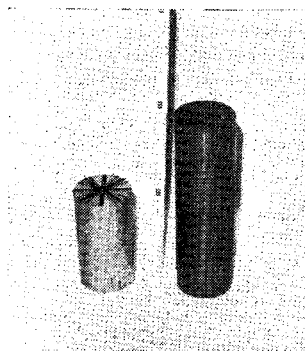


Photo. 2 Hole cutter (right) and rigid model cylinder (left).

(2) *Test for clay specimen containing model cylinder*

Excepting the operation of inserting model cylinder into clay specimen, same apparatus as described in (1) was used. At installing model cylinder a horizontal hole was previously opened in the clay specimen by a metal pipe (outer diameter

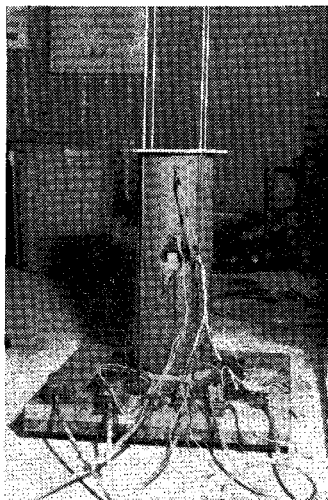


Photo. 3 Measuring apparatuses for impact test using rigid cylinder.

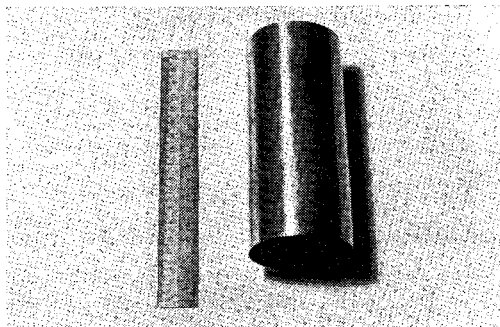


Photo. 4 Flexible model cylinder.

6 cm, thickness 0.5 mm and length 20 cm, see Photo. 2). The position of cylinder was at the depth of 20 cm from the top of the specimen. Very careful treatment was kept at installing the cylinder not so as to disturb the soft clay specimen.

Two kinds of model cylinder were used for this experiment; rigid cylinder and flexible one. The former was made of aluminium solid cylinder, weighted 840 g, diameter of 6 cm and length of 11 cm (on the left hand of Photo. 2). Photo. 3 indicates the apparatus installed with the rigid cylinder and the pressure gauges in the clay specimen around it. On the other hand, the latter was a thin-walled metal pipe, weighted 156 g, outer diameter of 6 cm, thickness of 0.5 mm and length of 14 cm (Photo. 4). Inside of the cylinder strain gauges were tapped at the crown and the side, and a small accelerometer (Photo. 5) was placed at the bottom of cylinder (Fig. 7).

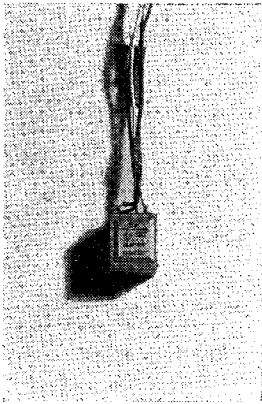


Photo. 5 Accelerometer.

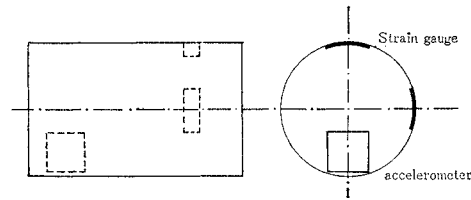


Fig. 7 Pick-ups set inside of flexible model cylinder.

Thus one can investigate the behavior of the model cylinder when the clay specimen was subjected to the impact loading. Photo. 6 shows the apparatus for this kind of test.

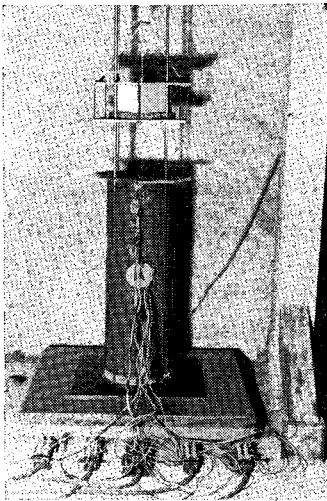


Photo. 6 Measuring apparatuses for impact test using flexible cylinder.

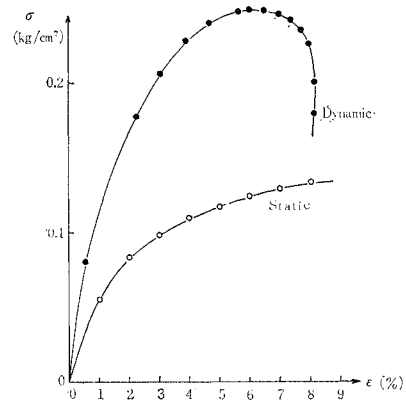


Fig. 8 Dynamic and static stress-strain curves.

3.2 Free Vibration Test

In order to get the stress-strain relationships of the clay specimen used in abovementioned impact test, a series of free vibration test was performed using the dynamic triaxial apparatus described elsewhere⁶⁾. Dynamic stress-strain curve was drawn from the displacement record and the load record, together with static curve indicated as Fig. 8. Average rate of strain in the dynamic test was $1.82 \times 10^4 \%$ /min.

4. ANALYSIS OF EXPERIMENTAL RESULT

4.1 Propagating Stress through Clay Specimen

(1) Applied surface pressure

Stress wave obtained by the pressure gauge situated at the position of 3 cm from the upper end of specimen was regarded as the applied surface pressure, when the falling weight of 1 750 g was dropped through a height of 70 cm. Averaged peak value of the applied surface pressures was 0.318 kg/cm^2 , the representative form being plotted on a semi-logarithmic paper as shown in Fig. 9. It is seen from this figure that after a rise time of 4 msec the stress wave decreases the intensity exponentially.

Mathematical expression of the decreasing part of the propagating stress as the function of time is $p(0, t) = p_0 e^{-230t}$ (t in sec), where p_0 denotes the peak intensity of the applied surface pressure.

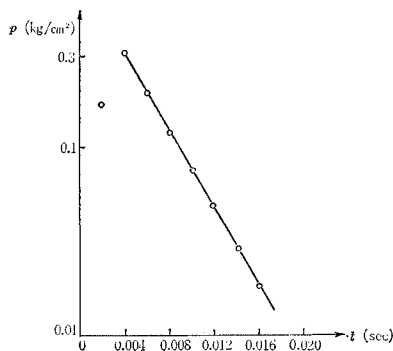


Fig. 9 Applied surface pressure.

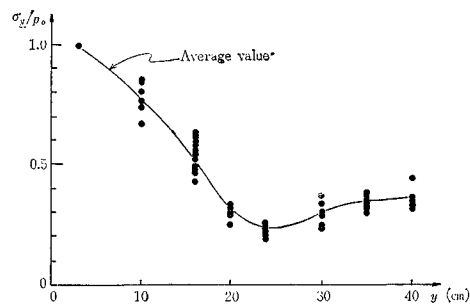


Fig. 10 Attenuation of peak stress with distance.

(2) Attenuation of the peak stress

Fig. 10 indicates the attenuation character of the peak stress with distance in a soil column. One can see the reflected wave at the end of column. As is seen in the figure the attenuation of stress is very large. It is due to the reason why the clay sample was very soft. Solid line in Fig. 10 shows the average value obtained in a series of test.

4.2 Dispersion of Stress Wave at the Surface of Model Cylinder

Small pressure gauges were set in the clay specimen as shown in Fig. 11 in order to investigate the stress distribution around the model cylinder. The distance between the gauges and the cylinder was 1 cm.

The region $90^\circ \leq \theta \leq 180^\circ$ (the angle θ measured from the bottom of cylinder) is called the *illuminated zone* where stress characters are distinguished from the *shadow zone*, $0^\circ \leq \theta \leq 90^\circ$. It is to say that the former is directly subjected to the stress wave, while the latter has no direct influence of the wave as it is situated behind the buried structure. If the cylinder is perfectly fixed in the clay specimen, therefore, there occurs no instantaneous stress just after the impact loading, but a gradual occurrence of stress by refraction. Provided the cylinder is not perfectly fixed, on the other hand, which corresponds to the actual condition between ground and structure, some passive stress generates in the shadow zone due to the movement of cylinder. In the present experiment the model cylinder was in the latter case.

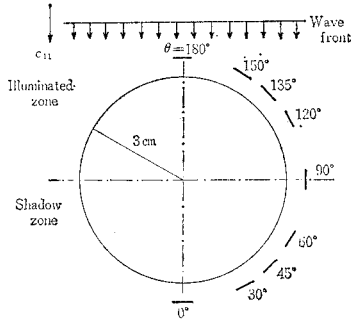


Fig. 11 Installation of pressure gauges around model cylinder.

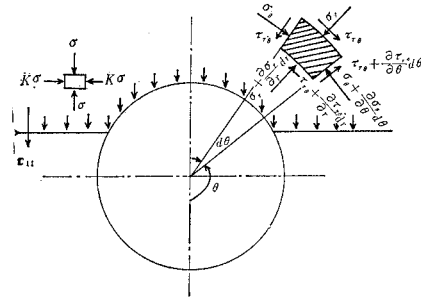


Fig. 12 State of stress behind wave front.

As is indicated in Fig. 12, the state of stress in the clay specimen behind the wave front is vertically the compressive stress σ and horizontally $K\sigma$, where $K = \nu/(1-\nu)$ (ν : Poisson's ratio) denotes the coefficient of lateral earth pressure. Thus the incident radial stress to the cylinder $\sigma_r^{(i)}$ can be expressed as:

$$\sigma_r^{(i)} = \sigma_e (\cos^2 \theta + K \sin^2 \theta) \quad (22)$$

where, σ_e denotes the normal stress at the crown of cylinder, $\theta = 180^\circ$.

When the lateral confinement is free, we can take $K=0$, thus,

$$\sigma_r^{(i)} = \sigma_e \cos^2 \theta \quad (23)$$

Fig. 13 shows schematically the reflection mechanism of the stress wave at the surface of model cylinder. It can be understood that the measured wave pattern on a pressure gauge installed at the position (r, θ) is the superposition of the following three kinds of stress;

- 1) Directly incident stress wave (1) to the pressure gauge P is shown by the wave a in Fig. 13. Since the gauge has an inclination angle $(180^\circ - \theta)$ from the proceeding direction of stress wave, the normal component to the surface of gauge is recorded and the magnitude is given by Eq. (23).
- 2) Dilatational stress wave (2) entering to a point A on the cylinder with an incident angle η_p produces a reflected dilatational wave b with a reflecting angle λ_p is recorded on the pressure gauge P at the point (r, θ) . Reflected distortional wave starting from point A does not pass through the point P.

3) Similarly dilatational stress wave (3) entering to a point B on the cylinder with another incident angle η_s produces a reflected distortional wave c with a reflecting angle λ_s and is recorded on P. Reflected distortional wave starting from point B does not pass through the point P.

Thus in order to separate the incident stress (1) and the reflected stresses (2)+(3), it is necessary to find out the isolated value of (1) from the impact test for clay specimen which does not contain the model cylinder. The difference of these two kinds of test gives us the influence of reflected waves.

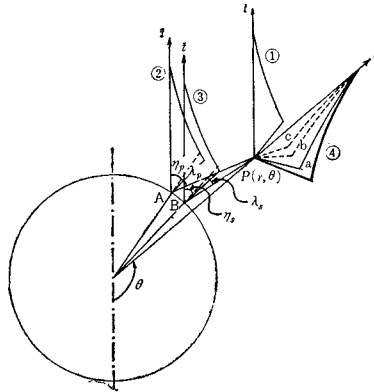


Fig. 13 Reflection of stress wave at the surface of model cylinder.

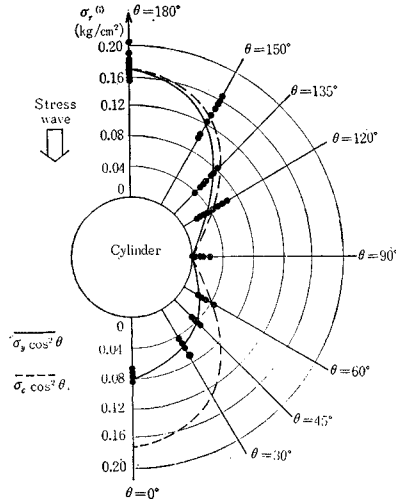


Fig. 14 Radial incident stresses to model cylinder.

4.3 Consideration of Incident Wave

(1) Radial incident wave

In order to obtain the intensity of incident wave, pressure gauges were located at the situations in the clay specimen as shown in Fig. 11, where in this case the model cylinder did not actually exist but was assumed as if the centre were located at the depth of 20 cm from the top of specimen. The gauges were arranged so that the normal to gauge surfaces passed through the postulated centre of model cylinder.

The plots in Fig. 14 indicate the peak stresses obtained in a series of this test. If there were no attenuation in the incident wave between the crown of assumed cylinder ($\theta=180^\circ$) and the bottom ($\theta=0^\circ$), the theoretical equation is given by Eq. (23). It is shown by the dotted line in Fig. 14 indicating symmetrical form about the horizontal axis through the centre of cylinder. Actually one can recognize a remarkable attenuation of propagating stress between the crown and the bottom, especially in the region of $0^\circ \leq \theta \leq 90^\circ$. The solid line in Fig. 14 corresponds to the theoretical value of the radial incident stress $\sigma_r^{(i)}$ calculated from the vertical stress σ_y at each position of the pressure gauges by the attenuation character of peak stress ever shown in Fig. 10;

$$\sigma_r^{(i)} = \sigma_y \cos^2 \theta \tag{24}$$

Accordance of measured stresses with this theoretical value is fairly well.

(2) *Tangential incident wave and shear incident wave*

Similarly as the abovementioned radial incident stress, $\sigma_r^{(i)}$, given by Eq. (24), the tangential stress, $\sigma_\theta^{(i)}$, and the shear stress, $\tau_{r\theta}^{(i)}$, are expressed by the following equations, considering the free lateral confinement and the attenuation of stress wave in the clay specimen:

$$\left. \begin{aligned} \sigma_\theta^{(i)} &= \sigma_y \sin^2 \theta \\ \tau_{r\theta}^{(i)} &= \sigma_y \cos \theta \sin \theta \end{aligned} \right\} \quad (25)$$

4.4 Dynamic Behavior of Cohesive Soil around Rigid Model Cylinder

(1) *Stress distribution in soil around model cylinder*

Fig. 15 shows the measured value of the radial stresses in the clay specimen around the rigid model cylinder, together with the incident stress $\sigma_r^{(i)}$ given by Eq. (24) and the total stress σ_r calculated from the second equation of Eq. (6) and the first equation of Eq. (21). Remarkable influence of the reflected wave can be recognized at the crown of cylinder in the illuminated zone. The experimental results in this zone are in pretty good accordance with the theoretical values for $\nu=0$ which corresponds to the boundary condition of no lateral confinement.

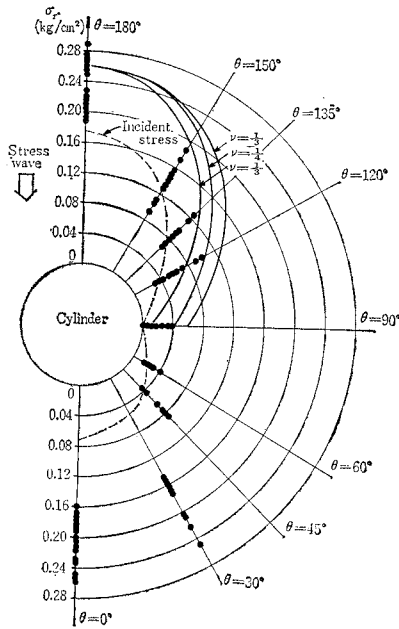


Fig. 15 Distribution of radial stresses around a rigid model cylinder.

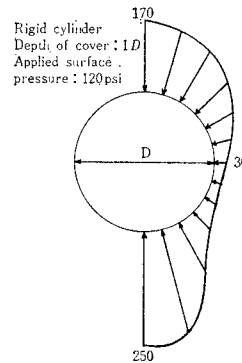


Fig. 16 Distribution of static pressure around a rigid model cylinder (after Höeg).

In the shadow zone, on the other hand, one can take notice of very large stresses behind the model cylinder. This phenomenon shows the effect of passive pressure in the soft soil surrounding a rigid structure. We can conclude that the distribution of the radial stress σ_r in the clay specimen around a rigid cylinder

is symmetrical to the horizontal axis through the centre of cylinder. The stress magnitude at the position of crown ($\theta=180^\circ$) is about 1.4 times (theoretically 1.54 times) that obtained in the test specimen which does not contain model cylinder, and about three times at the bottom of cylinder. This is an important result of dynamic interaction between soil and structure, but such a behavior has also been recognized in the static test performed by Höeg⁷⁾ (see Fig. 16).

The tangential total stress σ_θ and the shear total stress $\tau_{r\theta}$ can be obtained by using Eqs. (6) and (21).

(2) Transit time

The time required for stress wave to pass through a certain distance is called the transit time. Let us consider the transit time between the crown and the bottom of model cylinder, buried in a clay specimen.

In the case of clay specimen not containing the model cylinder, it took about 2.3–3.5 msec between the positions of pressure gauges corresponding to the crown and the bottom (8 cm). Thus the velocity of wave front c is about 22.8–33.8 m/sec, while from the theoretical value given by

$$c = \sqrt{\frac{E_0}{\rho}} \quad (26)$$

E_0 : initial modulus of elasticity, ρ : the density of medium

becomes $c=25.0$ m/sec, so that both values are fairly identical with each other.

When the clay specimen contains a model cylinder, on the other hand, the velocity of wave front increases extremely. In this case we have $c=40-400$ m/sec.

4.5 Dynamic Behavior of Cohesive Soil around Flexible Model Cylinder

(1) Stress distribution in soil around model cylinder

In the case of flexible model cylinder we have a quite different pattern of stress distribution around the cylinder compared with the case of rigid one described above. Now correlations between the incident wave and the reflected wave no longer hold there, thus the phenomena can be recognized by considering the deflection of cylinder.

In Fig. 17 are plotted experimental values of radial stress σ_r measured at each position around the model cylinder. Broken line in the figure showing $\sigma_y \cos^2 \theta$ corresponds to the free field stress which was obtained by the test for the specimen not containing cylinder.

Comparing this results with those in Fig. 15, one can point out the following three different characters:

- 1) Radial stress in the clay specimen around a flexible cylinder distributes almost uniformly along the circumference of the cylinder.
- 2) The stress at crown of the flexible cylinder is approximately half that in the case of the rigid cylinder and even smaller than the free field stress.
- 3) The stress at both sides of the flexible cylinder is considerably larger than that in the case of the rigid cylinder.

Above tendencies have been obtained by Höeg's static interaction test as shown in Fig. 18⁷⁾.

We can explain the abovementioned characters 2) and 3) as follows. As de-

scribed later the first mode of deflection of the flexible cylinder is elliptic as shown in Fig. 19. At the crown the cylinder deforms toward inside and there occurs arching in the soil neighbouring the crown, thus diminishing stresses. The opposite case can be considered at the sides of cylinder, establishing the soil reaction which is proportional to the magnitude of deflection.

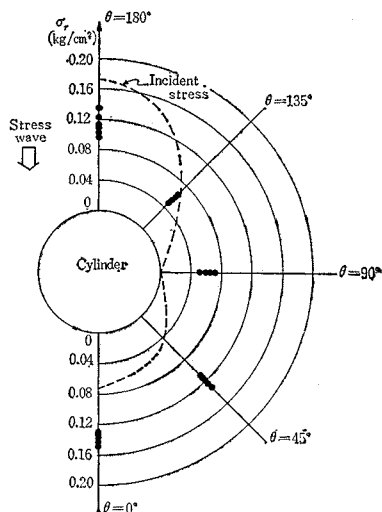


Fig. 17 Distribution of radial stresses around a flexible model cylinder.

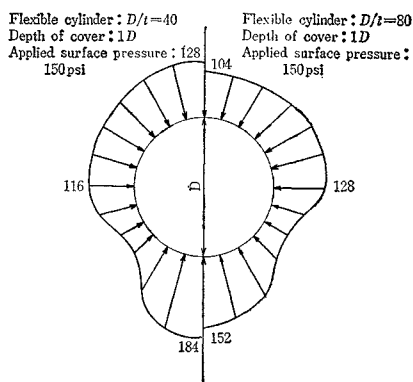


Fig. 18 Distribution of static pressure around a flexible model cylinder (after Höeg).

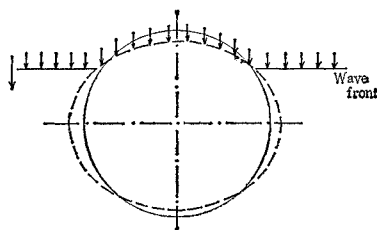


Fig. 19 First mode of deflection of a flexible cylinder.

By virtue of these two reasons the clay prevents the deformation of cylinder, thus making the stress distribution almost uniformly⁸⁾.

(2) Deflection of model cylinder

As described above it has been clear that the stress distribution in the clay specimen around a flexible cylinder greatly depends upon the rigidity or deflection of cylinder. Here we investigate the relationship by the measured value of strain gauge attached to the inside surface of the model cylinder. Fig. 20 illustrates one of the test results on the strains at the crown and the side of cylinder and on the stresses in the clay specimen around the cylinder. The strains have the maximum values after the rise time of about 15 msec. From this we can calculate the deflection of vertical and horizontal diameters of cylinder as approximately 0.8 mm and 1.0 mm, respectively.

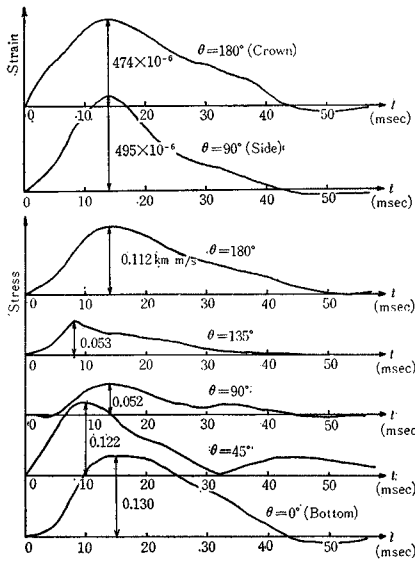


Fig. 20 Strain record and stress record.

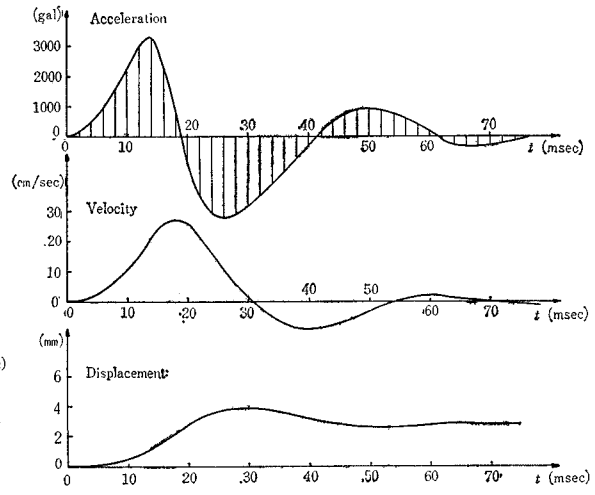


Fig. 21 Dynamic displacement of model cylinder obtained from acceleration record.

(3) Movement of model cylinder

It seems to be of great importance to investigate the manner that the cylinder moves downward with surrounding soil when it is subjected to a shock wave. In the present research a trial effort has been performed to find the movement of model cylinder by integrating the measured record of accelerometer which was set in the cylinder itself. The relationship between the acceleration \ddot{y} and the dynamic displacement y is expressed as:

$$y = \iint \ddot{y} dt dt \tag{27}$$

Taking the origin of time as the instance when the stress wave has reached the crown of cylinder, the initial conditions become $t=0: \dot{y}=0$ and $y=0$. Therefore we can integrate twice the acceleration record \ddot{y} with respect of time t to obtain the dynamic displacement y as indicated in Fig. 21. From this figure one can recognize that the maximum settlement of the model cylinder is approximately 4.0 mm, appearing at about 30 msec after the stress wave has reached the crown. As time elapses the settlement gradually gains the recovery with some oscillation, finally amounting to about 3.0 mm.

As is already stated, stresses and deformation of cylinder had the rise time of about 15 msec, whereas the maximum settlement was reached after about 30 msec from the incidence of stress wave to the crown. This means that the whole settlement of model cylinder occurs considerably slowly. The theoretical explanation of this behavior is not yet given in the present stage of this research.

4.6 Consideration on the State of Stress in Cohesive Soil around the Model Cylinder

From the result of a series of stress propagation test described in this section,

we are now able to investigate the state of stress in cohesive soil around the model cylinder. In general the state of stress in a medium can be expressed by Mohr's circle when the principal stresses or the stress components at a given point are known. In the present case the authors have confirmed that the measured radial stress σ_r in cohesive soil around the model cylinder fairly coincides with that obtained from the stress propagation theory, considering the reflection of stress wave at the surface of cylinder. It may be allowed, therefore, that the another components of stress, σ_θ and $\tau_{r\theta}$, expressed by the theory are similarly acceptable to us with considerable precision.

On the other hand, the undrained shear strength of cohesive soil is obtained by the unconfined compression test of which result is in some extent dependent of the rate of loading. The test result has shown that the dynamic unconfined compressive strength is about one and half times or twice the static one (see Fig. 8).

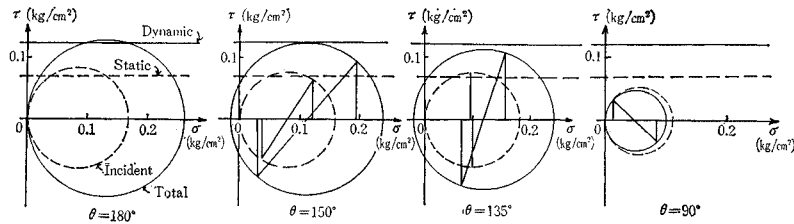


Fig. 22 Mohr's τ - σ plane for the model test.

Representation of the state of stress on Mohr's τ - σ plane for the model test of stress propagation through cohesive soil containing a cylinder is shown in Fig. 22. In this figure the dotted circles correspond to the incident stress at each position in the so-called illuminated zone around the model cylinder obtained from the measured result and also by theoretical equations (24) and (25). The solid circles mean the total stress circles, *i.e.* the incident stress plus the reflected one, on the other hand, obtained from experimental data and by using Eqs. (6) and (21). Broken straight line in the figure shows the undrained shear strength of clay used in the test under the static condition, whereas the full line corresponds to that under dynamic condition. Both failure lines are obtained from the test results shown in Fig. 8, the latter being the case of the stress propagation test.

From Fig. 22 it is clear that the approach of plastic failure under dynamic condition is severely established at the position between $\theta=150^\circ$ and $\theta=180^\circ$ which corresponds to the upper half of the illuminated zone. At the side part of the buried cylinder, $\theta=90^\circ$ - 135° , on the other hand, the state of stress caused by the shock disturbance is pretty mild. Therefore, it seems that there exists little approach to plastic failure under dynamic condition.

5. CONCLUSIONS

Throughout the above investigations described in this paper, some important conclusions can be obtained and are summarized as follows:

- (1) The incident wave caused by a shock disturbance at the upper surface of clay column indicates a remarkable attenuation of propagating stress.

(2) When the incident wave runs to the neighbourhood of a rigid model cylinder, the radial stress σ_r in the clay specimen at the position of crown is about 1.4 times that obtained on the test specimen which does not contain model cylinder, and about 3 times at the bottom of cylinder.

(3) In the case of a flexible cylinder, on the other hand, the radial stress at the crown is approximately half that in the case of rigid cylinder and even smaller than the free field stress. The stress at the side part is considerably larger than that in the case of rigid cylinder.

(4) Cohesive soil surrounding the model cylinder is in a close relation to the deformation of cylinder. The whole settlement of model cylinder occurs with some time lag, independently of the cylinder deformation and the stress state around it.

(5) The approach of plastic failure in cohesive soil surrounding a rigid cylinder is severely established in the upper half of the illuminated zone. At the side part of the buried cylinder, on the other hand, the state of stress caused by the shock disturbance is pretty mild.

REFERENCES

- 1) Yamada, G.: Damage to Earth Structures and Foundations by the Niigata Earthquake June 16, 1964 in JNR, Soils and Foundations, Vol. 6, No. 1, 1966, pp. 1-13.
- 2) Baron, M. L. and R. Parnes: Diffraction of a Pressure Wave by a Cylindrical Cavity in an Elastic Medium, J. Appl. Mech., Vol. 28, Series E, 1961, pp. 347-354.
- 3) Kolsky, H.: Stress Waves in Solids, Dover Publ., N.Y., 1963, pp. 4-16.
- 4) U.S. Air Force Special Weapons Center: A Theoretical Analysis of Stress Wave Interaction in a Model Soil, Report No. AD-411367, 1963, pp. 84-92.
- 5) Akai, K., Tokuda, M. and T. Kiuchi: Experimental Study on the Propagation of Stress Wave in Cohesive Soils, Proc. JSCE, No. 161, 1969, pp. 59-67.
- 6) Akai, K. and Y. Yamauchi: Response Characteristics of Saturated Clay to Impact Loading, Soils and Foundations, Vol. 8, No. 2, 1968, pp. 13-34.
- 7) Höeg, K.: Stress against Underground Structural Cylinders, J. ASCE, Vol. 94, No. SM4, 1968, pp. 833-858.
- 8) Marino, Jr. R. L. and W. F. Riley: Response of Buried Structural Models to Static and Dynamic Overpressures, Proc. Symp. Soil-Structure Interaction, 1964, pp. 464-486.

APPENDIX Cylindrical Divergence Coefficients and Reflection Coefficients

Cylindrical divergence coefficients

The significance of the cylindrical divergence coefficient means the rate of divergence of the reflected deformation potential at the point of observation to the magnitude of that at the surface of cylinder. Such a consideration is necessary in treating the problem, in which a stress wave runs to a curved surface such as cylinder, not to a plane surface.

Referring Fig. A-1, consider two parallel rays penetrating into a medium at the neighbourhood of a rigid cylinder. They diverge as the reflected rays A and B as shown in the figure.

The area dS at the surface of an assumed arc with radius f surrounding the reflected rays A and B is

$$dS = f d\alpha$$

This infinitesimal area contains n rays and each of them diverges with a flux density

$$\gamma_f = \frac{n}{dS} = \frac{n}{f d\alpha}$$

Similarly, on the surface of another arc with radius $f + R_p$,

$$\gamma_{f+R_p} = \frac{n}{dS'} = \frac{n}{(f + R_p) d\alpha}$$

Thus the ratio of flux densities at the point of observation to at the surface of cylinder is

$$\frac{\frac{n}{dS'}}{\frac{n}{dS}} = \frac{dS}{dS'} = \frac{f}{f + R_p}$$

Therefore, the above ratio is the reciprocal of the area ratio, and the ratio of flux densities in terms of the corresponding length is

$$D_{pp} = \sqrt{\frac{f}{f + R_p}}$$

Similarly,

$$D_{ps} = \sqrt{\frac{g}{g + R_s}}$$

(17)

Reflection coefficients

The reflection coefficient R_{pp} expresses the ratio of intensity of the reflected stress to that of the incident stress. Using Snell's law (13) and replacing θ_1 , θ_2 and θ_3 in Eq. (14) as:

$$\theta_1 = \eta_p, \quad \theta_2 = \lambda_p', \quad \text{and} \quad \theta_3 = \lambda_p$$

one obtains

$$\begin{aligned} R_{pp} = \frac{A}{p} &= \frac{\cos(\theta_1 + \theta_2)}{\sin \theta_1 \sin \theta_2 + \frac{c_{11}}{c_{12}} \cos \theta_2 \cos \theta_3} = \frac{\cos(\eta_p + \lambda_p')}{\sin \eta_p + \sin \lambda_p' + \frac{c_{11}}{c_{12}} \cos \lambda_p' \cos \lambda_p} \\ &= \frac{\cos \eta_p \left\{ 1 - \left(\frac{c_{22}}{c_{11}} \right)^2 \sin^2 \eta_p \right\}^{1/2} - \frac{c_{22}}{c_{11}} \sin^3 \eta_p}{\frac{c_{22}}{c_{11}} \sin^2 \eta_p + \frac{c_{11}}{c_{12}} \left\{ 1 - \left(\frac{c_{22}}{c_{11}} \right)^2 \sin^2 \eta_p \right\}^{1/2} \left\{ 1 - \left(\frac{c_{12}}{c_{11}} \right)^2 \sin^2 \eta_p \right\}^{1/2}} \end{aligned} \quad (20)$$

For the coefficient R_{ps} a substitution is taken as:

$$\theta_1 = \eta_s, \quad \theta_2 = \lambda_s \quad \text{and} \quad \theta_3 = \lambda_s'$$

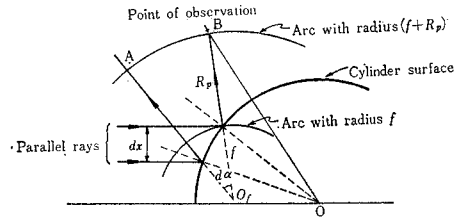


Fig. A-1 Explanation of the cylindrical divergence coefficient, D_{pp} .

(Received June 17, 1969)

- 高い粘性によるコストダウン
- 高い膨潤
- 少ない沈澱
- 品質安定

業界に絶対信用ある…
山形産ベントナイト
基礎工事に用泥水に

クニゲル



国峯砒化工業株式会社

本社 東京都中央区新川1-10 電話(552)6101代表
工場 山形県大江町左沢 電話 大江 2255-6
鉱山 山形県大江町月布 電話 貫見 14

代理店

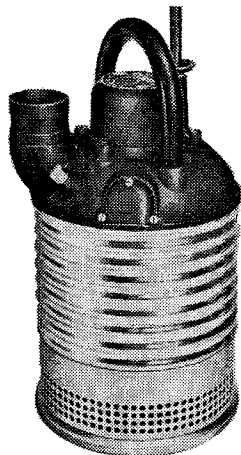
ベントナイト産業株式会社

東京都港区新橋2-18-2 電話 東京 (571)4851-3

機動性と安全性の追求

特許

クインテックス 水中ポンプ



- 重量・他社ポンプの1/3
 - 移設費・仮設費ゼロ!!
 - 連続ドライ運転OK!!
- (特許空冷バルブ装備)

〈御一報次第資料送呈〉

型 式	口 径 in	重 量 kg
19H型	6, 4	140
19 型	8, 6	140
5 H型	4, 3	48
5 型	6, 4	40
3 型	4, 3	35
2 型	3, 2½	23
1 型	2½, 2	17

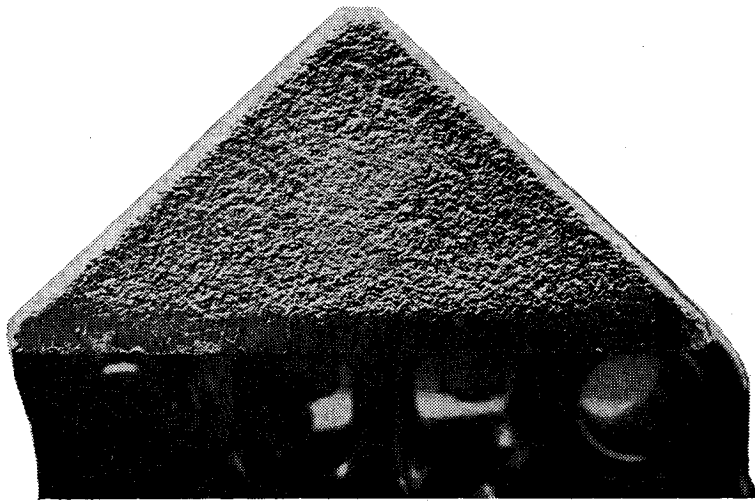
総発売元

ラサ商事株式会社

本 社 東京都中央区日本橋茅場町1の12 ☎103 電話 東京 (03)668-8231
支店・営業所 大阪・札幌・仙台・名古屋・福岡・東京機械工場

NTKが

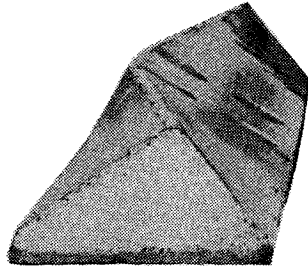
正統派です



二等辺直角三角形の純正NTK三角シュー

悪質地盤の処理に抜群の働きを示す湿地ブルドーザは、日本のユーザーにとって欠かせない機動力であることはご承知の通りですが、その普及の目覚ましきにつれて、あるメーカーが「日本No.1の技術が開発した」といえば、一方は「世界No.1の技術が...」とうたう。しかし、一寸待って下さい。湿地ブルドーザの生命である三角シューは、北海道の泥炭地と取組んだ日特金属が発明したものです。それまでシューは、グロウサシかなかったのです。日特の開発した三角シューは、土がつかず、土を乱さず、転圧力が大きく、傾斜地にも強いという画期的な性能を備えており、日本のユーザーの要望に完全に応えたもの。そして湿地研究から生まれた頑強な足廻り、理想の車体バランス等正統派NTKの湿地ブルドーザは断然ピカイチです。超々湿地ブルまで種類も豊富。湿地ブルについては専門家のNTKにまずご相談下さい。

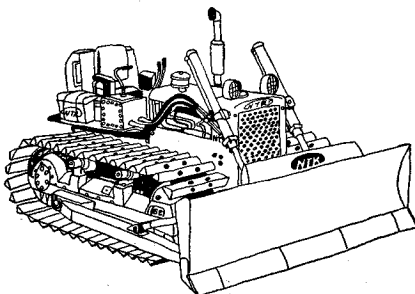
三角シューのいろいろ



稜線にカーブをつけた三角シュー



側面に丸味をつけた三角シュー



豊富な湿地シリーズ	接地圧	定格出力	総重量
NTK-6C 湿地	0.29kg/cm ²	120ps	15,000kg
NTK-5 湿地	0.27kg/cm ²	76ps	9,200kg
NTK-5 超湿地	0.19kg/cm ²	76ps	10,300kg
NTK-5 超々湿地	0.13kg/cm ²	76ps	10,000kg
NTK-4 湿地	0.25kg/cm ²	61ps	8,100kg

NTK
日特金属工業株式会社
 東京都田無市谷戸町2-1-1 ☎0424 (63) 2121